pH and lipase-responsive nanocarrier-mediated dual drug delivery system to treat periodontitis in diabetic rats

Lu Wang [a,b], Yuzhou Li [a,c], Mingxing Ren [b,c], Xu Wang [a,c], Lingjie Li [c], Fengyi Liu [a], Yiqing Lan [b,c], Sheng Yang [a,b,c,**], Jinlin Song [a,b,c,*]

[a] *College of Stomatology, Chongqing Medical University, Chongqing, China*
[b] *Chongqing Key Laboratory of Oral Diseases and Biomedical Sciences, Chongqing, China*
[c] *Chongqing Municipal Key Laboratory of Oral Biomedical Engineering of Higher Education, Chongqing, China*

ARTICLE INFO

ABSTRACT

Precise and controlled drug delivery to treat periodontitis in patients with diabetes remains a significant clinical challenge. Nanoparticle-based drug delivery systems offer a potential therapeutic strategy; however, the low loading efficiency, non-responsiveness, and single effect of conventional nanoparticles hinder their clinical application. In this study, we designed a novel self-assembled, dual responsive, and dual drug-loading nanocarrier system, which comprised two parts: the hydrophobic lipid core formed by 1, 2-Distearoyl-sn-glycero-3-phosphoethanolamine-Poly (ethylene glycol) (DSPE-PEG) loaded with alpha-lipoic acid (ALA); and a hydrophilic shell comprising a poly (amidoamine) dendrimer (PAMAM) that electrostatically adsorbed minocycline hydrochloride (Mino). This unique design allows the controlled release of antioxidant/ALA under lipase stimulation from periodontal pathogens and antimicrobial/Mino under the low pH of the inflammatory microenvironment. *In vivo* and *in vitro* studies confirmed that this dual nanocarrier could inhibit the formation of subgingival microbial colonies while promoting osteogenic differentiation of cells under diabetic pathological conditions, and ameliorated periodontal bone resorption. This effective and versatile drug-delivery strategy has good potential applications to inhibit diabetes-associated periodontal bone loss.

1. Introduction

Diabetes mellitus (DM) and its related complications are a serious threat to global health [1,2]. Periodontitis, considered as the sixth complication of diabetes, is negatively affected by metabolic disorders and related pathological status in DM [3,4]. It has been reported that DM potentiates the severity of the local inflammation induced by dental plaque [5–7], which is the initiating factor for periodontitis and permanently exists in the periodontal environment (mainly the gingiva, periodontal ligament, and alveolar bone). Moreover, hyperglycemia status and resultant advanced glycation end product (AGE) formation could induce reactive oxygen species (ROS) accumulation, exacerbate inflammation, and impair the differentiation of osteoblasts, resulting in more rapid and severe destruction of periodontal bone [8,9]. However, the conventional clinical therapies for periodontitis (mainly mechanical debridement and surgical periodontal treatment [10]) do not consider

the specific microenvironment of diabetes, and are limited in achieving satisfactory therapeutic effects. Therefore, there is an urgent need to develop a novel strategy to implement personalized measures to treat periodontitis under diabetic conditions.

Nanoparticle (NP)-based drug delivery systems, mainly including liposomes [11–13], polymeric NPs [14,15], metallic NPs [16,17], and inorganic NPs [18,19], are considered as a promising and effective treatment strategy for bone regeneration [20,21]. It is well known that with the advantages of improving drug solubility, decreasing toxicity, increasing drug stability, and reducing drug decomposition, nano-drug delivery systems can utilize special microenvironmental changes to achieve controlled and programmed drug release, and play an important role in immune regulation, antibacterial and anti-inflammatory activities [22–25]. For example, Zhao et al. designed a novel nano neuro-immune blocker capsule that could exploit the photothermal effect under near infrared (NIR) irradiation to enhance the innate immune

response [17]. In another study, a smart NIR-light-controlled drug release of a black phosphorus/gold nanocomposite was developed to disrupt biofilm formation [16]. However, there are several limitations of these nanoscale delivery systems in periodontal tissues under diabetic conditions. Firstly, the high level of ROS and oxidative stress in DM aggravate the immune response and inflammation [7,26,27], which might require smarter nanocarriers that encapsulate multiple drugs and exert multiple effects at the same time in this specific microenvironment. Moreover, the physiological properties (the rapid scouring effect of saliva) around periodontal tissues lead to low drug accumulation at periodontal local bone defect sites, which greatly compromises the therapeutic effect of nanocarriers. Therefore, designing a precise and controllable multi-drug-loaded nanocarrier to simultaneously acquire antibacterial, antioxidative, anti-inflammatory, and osteoinductive functions for diabetic microenvironments is the key to realizing personalized measures to treat periodontitis in DM.

Under diabetic conditions, dental plaque and the inflammatory microenvironment are both acidic (pH 4.5–6.5) [28–31], providing a potential stimulus and an ideal target for pH-responsive carriers. Many studies reported that Poly (amidoamine) (PAMAM) is pH-sensitive because of its loose structure under weakly acidic conditions [32,33], which could be exploited to trigger drug release, and thus could be widely used for responsive release in acidic environments. In addition, PAMAM is an excellent nanosized platform for drug delivery in numerous applications [34–36] because of its specific structure, such as the interior hydrophobic region, a large number of end amino groups, and narrow size distribution [37–41]. Moreover, many bacterial enzymes (e.g., esterase, lipase, and gelatinase) exist in dental plaque [29, 42,43] and can be exploited to achieve enzyme-mediated drug release. 1,2-Distearoyl-sn-glycero-3-phosphoethanolamine-Poly (ethylene glycol) (DSPE-PEG), a PEGylated lipid polymer, is sensitive to bacterial enzymes (e.g., lipase). It can also increase the solubility of a poorly soluble drug and improve the drug loading capacity [44,45].

Inspired by the features of diabetic periodontal microenvironment (pathogens, low pH, high level of ROS, and bone loss)and the superior features of DSPE-PEG and PAMAM, we have developed a novel pH and lipase dual response nanocarrier system constructed from two components: a hydrophobic lipid core (DSPE-PEG) loaded with alpha-lipoic acid (ALA), which is an anti-oxidative, anti-inflammatory, and osteoinductive agent [46], and a hydrophilic dendrimer shell (PAMAM) encapsulating minocycline hydrochloride (Mino), a broad-spectrum antibiotic commonly used in clinical periodontal treatment. These two-part block copolymers were named as DPPLM NPs. Upon exposure to acidic conditions at the presence of lipase *in vitro*, a pH-responsive

release of Mino and a lipase-responsive release of ALA were triggered. Moreover, the functions of enhanced osteogenic, antioxidant, anti-inflammatory, and antibacterial activities of the DPPLM NPs were determined *in vitro*. Furthermore, these NPs exhibited outstanding performance in destroying dental plaque and further preventing periodontal bone loss in an experimental periodontitis model in DM rats (Scheme 1). Overall, this study provided an effective therapeutic strategy to inhibit periodontal bone loss in DM.

2. Materials and methods

2.1. Reagents and materials

A fourth-generation poly (amidoamine) dendrimer (G4.0 PAMAM)) was obtained from Chenyuan Molecular (Weihai, Shandong, China). 1,2-distearoyl-sn-glycero-3-phosphoethanolamine-*N*-[succinimidyl (polyethylene glycol)-2000] (DSPE-PEG$_{2000}$-NHS) was obtained from Ponsure Biotechnology (Shanghai, China). The Cell Counting Kit 8 (CCK8), and Lyso-Tracker Green were supplied by Beyotime Biotechnology (Shanghai, China). The Alizarin Red Staining Kit was bought from Solarbio Science & Technology Co. (Beijing, China). Fluorescein isothiocyanate (FITC), Nile Red, Rhodamine B (Rho B), ALA, dimethyl sulfoxide (DMSO), and Streptozotocin (STZ) were purchased from Sigma-Aldrich (St. Louis, MO, USA). The collagen membrane was obtained from Geistlich Pharma AG (Wolhusen, Switzerland). AGE glycated bovine serum albumin (AGE-BSA) was bought from Abcam (Cambridge, MA, USA), Mino was purchased from AbMole Bioscience (Houston, TX, USA). Primary antibody for inducible nitrous oxide synthase (iNOS) were obtained from Santa Cruz Biotechnology (Santa Cruz, CA, USA). The TRIzol reagent and reverse transcription kit were bought from Invitrogen (Carlsbad, CA, USA) and Takara Shuzo (Kyoto, Japan). All other reagents and products for cell culture were bought from GIBCO (Gaithersburg, MD, USA) unless otherwise stated.

2.2. Synthesis and characterization of DPP and DPPLM NPs

The blank polymers were synthesized using the diafiltration method. Briefly, DSPE-PEG$_{2000}$-NHS was dissolved in DMSO (2 mL) and then added dropwise into 8 mL of deionized water under magnetic stirring at 25 °C for 4 h. PAMAM was dissolved in 2 mL of deionized water. Then, the DSPE-PEG and PAMAM solutions were mixed and stirred gently at 25 °C overnight. The primary amino groups on the surface of PAMAM reacted specifically with the terminal NHS group of the PEG derivative (groups were covalently conjugated to the DSPE-PEG$_{2000}$-NHS through
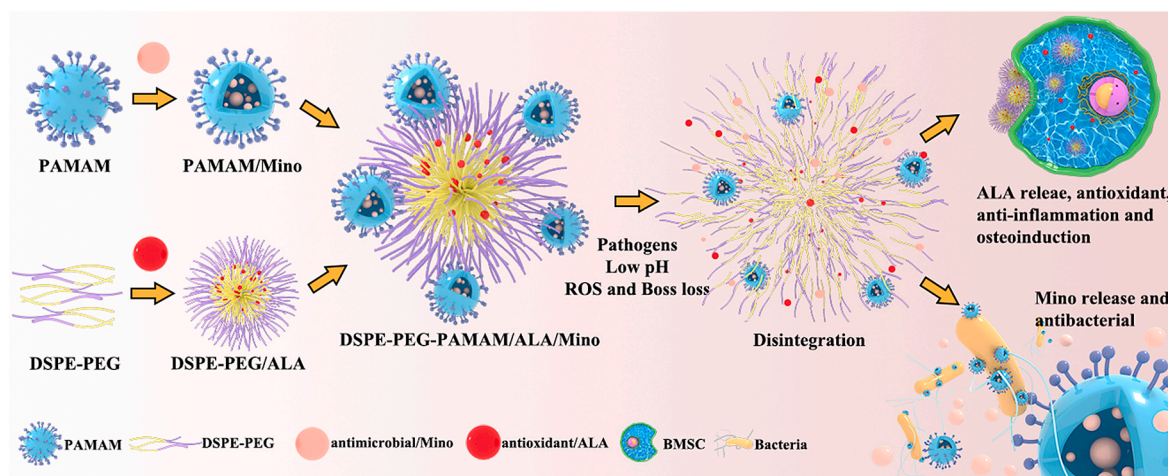
Scheme 1. Schematic illustration of engineering for DPPLM NPs. The nanocarrier system could simultaneously and efficiently carry and intelligently release two specific active drugs at periodontal bone defect sites of diabetic rats, and subsequently destroy dental plaque and ameliorate periodontal bone resorption. ALA, alpha-lipoic acid; Mino, minocycline hydrochloride; DPPLM NPs, DSPE-PEG-PAMAM/ALA/Mino nanoparticles.

an effective Michael addition reaction to obtain the final modified dendrimers). After the reaction was completed, the reaction solution was dialyzed in a dialysis bag (molecular weight cut off (MWCO) = 50 KDa) against deionized water for 72 h at 25 °C. The water was changed every 3 h. Finally, the DSPE-PEG-PAMAM nanoparticles, named DPP NPs for short, were obtained after freeze-drying, and stored at −20 °C. The drug-loaded, Nile red-loaded, and Rho B-loaded nanoparticles were prepared using the same procedure described above. ALA was added at weight ratios of ALA:PAMAM = 4:24.26, 8:24.26, and 16:24.26. Mino was added at a weight ratio of PAMAM:Mino = 24.26:16. The grafting ratio of DSPE-PEG on the exterior of the PAMAM was measured using the following formula based on ^{1}H nuclear magnetic resonance (NMR) spectra in deuterium oxide (D$_2$O): a × n/b = c, p = n/64 × 100%, where a is the average number of selected characteristic-H on PEG, b is the number of selected characteristic-H on PAMAM, c is the characteristic peak integral ratio of DPP, n is the average number of DSPE-PEG moieties successfully conjugated to PAMAM, and p is the PEGylation proportion of PAMAM. The size and morphology of empty and drug-loaded nanoparticles were monitored using dynamic light scattering (DLS, Brookhaven NanoBrook Omni, Brookhaven Instruments Corporation, Holtsville, NY, USA) and transmission electron microscopy (TEM, Hitachi-7500, Tokyo, Japan). The successful synthesis of nanoparticles was further confirmed by Fourier Transform Infrared spectroscopy (FTIR, Thermo Scientific Nicolet iS50, Thermo Scientific, Waltham, MA, USA).

2.3. In vitro drug loading

The drug loading content = (DLC, weight of loaded drug/weight of the drug loaded nanoparticles) × 100%, and drug loading efficiency = (DLE, weight of drug incorporated in assembled nanoparticles/weight of drug used in the fabrication) × 100% were determined using a UV–Vis scanning spectrophotometer. The calibration curves were acquired with different Mino concentrations at 280 nm in water and different ALA concentrations at 330 nm in ethanol.

2.4. In vitro drug release study

The drug responsive release characteristics were determined. Briefly, DPPLM (2 mg, 1 mg/mL) in a dialysis bag (MWCO = 50 KDa) was immersed in phosphate buffered saline (PBS; 20 mL) at pH 7.4, pH 5.5, pH 7.4 with 1 mg/mL lipase, and pH 5.5 with 1 mg/mL lipase, respectively. The release study was conducted in a thermotank under gentle shaking at 37 °C. Next, at certain times (0, l, 2, 4, 6, 8, 12, 24, and 48 h), 2.0 mL of dialysis fluid outside the bag was sampled and an equal amount of fresh release medium was supplied immediately to keep the same volume. The release amount was determined using a UV–Vis scanning spectrophotometer.

2.5. Cell culture

Bone marrow mesenchymal stem cells (BMSCs) were isolated from the long bones of 3 to 4-week-old female Sprague-Dawley (SD) rats. Following euthanasia using carbon dioxide inhalation suffocation, the femurs and tibiae were aseptically dissected and washed with PBS. The ends of the bones were cut off below the end of the bone marrow cavity and the marrow was flushed out from the bones using a 5 mL syringe with Dulbecco's modified Eagle's medium (DMEM) supplemented with 10% fetal bovine serum (FBS) at 37 °C in a 5% CO$_2$ atmosphere. Cells were centrifuged at 200×g for 5 min and resuspended in fresh DMEM. Cells were cultured in a humidified atmosphere with 5% CO$_2$ at 37 °C. Non-adherent cells were discarded and the medium was exchanged for the first time after 48 h. The adherent cells were detached using 0.25% trypsin/EDTA at day 7. At approximately 80% confluence, the cells were trypsinized and subcultured. The cells at passages 3–5 were used in the following experiments.

2.6. In vitro cellular uptake

Before the experiment, round slides were disinfected and placed in a 24-well plate. BMSCs were seeded into the 24-well plate at a density of 5000 cells per well and cultured for 24 h. Then, the medium was removed, and the cells were cultured with starvation medium (99% basal medium and 1% penicillin–streptomycin) for 12 h. Thereafter, the cells were incubated with 10 μg/mL DPP-FITC/Nile red and DPP-FITC/Rho B for another 2 h and 24 h, respectively. Thereafter, the cells were washed with PBS three times and fixed with 4% (v/v) para-formaldehyde. The nuclei were stained with 4′,6-diamidino-2-phenyl-indole (DAPI). Then, all cells were observed using confocal laser scanning microscopy (CLSM, Leica TCS SP8, Wetzlar, Germany).

2.7. In vitro cytotoxicity study

The in vitro cytotoxicity of DPPLM NPs was investigated using the CCK8 kit. Briefly, BMSCs were seeded in 96-well plates at 5000 cells per well with 100 μL of DMEM medium and cultured at 37 °C for 24 h. Then, the culture medium was replaced with 100 μL DMEM containing DPPLM NPs at different concentrations. After 24 h, 10 μL of CCK8 solution were added into each well. The absorbency of the solution was measured on a TECAN microplate reader at 450 nm (Tecan Group Ltd., Männedorf, Switzerland). The relative cytotoxicity rate was evaluated using the following formula:

Cell viability (%) = (A-B)/(C–B) × 100%

where A is the absorbance of the experimental group (containing cells, culture medium, CCK-8 solution, and nanoparticles solution), B is the absorbance of the blank group (with medium, CCK-8 solution, without cells, nanoparticles), and C is the absorbance of the control group (containing cells, culture medium, CCK-8 solution, without nanoparticles).

2.8. Subcellular localization

BMSCs were seeded into confocal dishes and incubated at 37 °C for 24 h, and then incubated with 10 μg/mL DPP/Nile red NPs for 20 min, 2 h, and 24 h at 37 °C. Next, the medium was removed and cells were washed with cold PBS three times, followed by staining with Lyso-Tracker Green for another 15 min. Hoechst 33342 was used to stain the nuclei. Then, all cells were observed using CLSM.

2.9. In vitro flow cytometry

BMSCs were seeded in 6-well dishes at 2 × 10^5 cells per well and incubated at 37 °C for 24 h. The medium was discarded and replaced with new DMEM containing 10 μg/mL DPP-FITC NPs and incubated for 24 h. Then, the medium was discarded and the cells were rinsed with PBS three times. The cells were trypsinized, collected by centrifugation, and then analyzed on a flow cytometer (BD FACSAria III, BD Biosciences, San Jose, CA, USA). Cells without any treatment were used as the blank control and named as the PBS group.

2.10. Hard tissue penetration of PAMAM

Fluorescently labeled PAMAM (PAMAM-FITC) was injected under the subcutaneous fascia of the calvarial bone of rats. The rats were sacrificed 5 days later and fluorescence scanning images of the bone were observed under a confocal microscope. To further determine that whether PAMAM could penetrate into the tooth root, the intact root was immersed in PAMAM-FITC solution for 5 min. After washing three times, the surface and cross section of the root were observed under a confocal microscope and a fluorescence microscope, respectively.

2.11. Osteogenic differentiation and detection

To investigate the effects of DPPLM NPs on the osteogenic differentiation of AGE-induced BMSCs, mineral deposition was detected. BMSCs were seeded in 24-well plates at a density of 5×10^4 cells per well. At approximately 80% confluence, the medium was discarded and replaced with osteogenic medium (OM; 10 mM β-glycerophosphate, 1 mM dexamethasone, and 50 μg/mL L-ascorbic acid-2-phosphate in complete medium). After 14 days of incubation in OM, Alizarin Red staining was performed to assess mineral deposits. For the quantitative analysis of mineralization, deposited calcium was eluted using 10% (w/v) cetyl-pyridinium chloride (Sigma-Aldrich), and the OD value was measured at 562 nm.

2.12. Quantitative real-time reverse transcription polymerase chain reaction (qRT-PCR) analysis

Total RNA was extracted using the Trizol reagent (Takara) and converted to cDNA using a PrimeScriptRT reagent kit (Takara). Then, the cDNA was used as the template for quantitative real-time PCR (qPCR) using SYBR Premix ExTaq II (Takara) on the CFX96PCR system (Bio-Rad, Hercules, CA, USA) to quantify gene expression. After incubation for 7 days, the osteogenic related genes including *Alp* (alkaline phosphatase), *Runx2* (runt-related transcription factor 2), *Ocn* (osteocalcin), *Opn* (osteopontin), and *Osx* (osterix) in BMSCs were measured using qRT-PCR. Sequences of the primers are presented in Table 2 (Supporting Information).

2.13. Intracellular ROS measurement

For ROS staining, the fluorescent probe 2,7-dichlorofluorescein diacetate (DCFH-DA) (Beyotime Institute of Biotechnology, Jiangsu, China) was used to test the level of ROS. Briefly, the cells were incubated with DCFH-DA (diluted to a final concentration of 10 μM) in PBS for 30 min in the dark. After rinsing with PBS three times, the cells were observed under a fluorescence microscope.

2.14. Immunofluorescence staining

After starvation for 12 h, BMSCs were incubated with serum-free medium containing 100 μg/mL AGE in the presence or absence of 100 μg/mL DPPLM NPs for 24 h. Then, the medium was discarded and cells were washed with PBS three times. Cells were fixed with 4% paraformaldehyde solution for 10 min, permeabilized with 0.2% TritonX-100 for 10 min, and blocked with 5% donkey serum at 37 °C for 1 h. After each step, the cells were rinsed with PBS three times. Then, mouse monoclonal *anti*-iNOS (1:300; sc-7271; Santa Cruz Biotechnology) antibodies were incubated with the cells at 4 °C for 12 h, and a fluorescence-conjugated anti-mouse secondary antibody (Alexa Fluor® 647; 1:500; Beyotime, Shanghai, China) was subsequently added to bind with the primary antibody. The nuclei were stained with DAPI. Finally, the cells were observed under a confocal laser scanning microscope.

2.15. In vitro antibacterial testing of DPPLM NPs

*Staphylococcus aureus (S. aureus) an*d *Escherichia coli (E. coli)* were chosen to evaluate the antibacterial ability using the broth microdilution method as described previously [42]. 100 μL of bacterial suspension was seeded in a 96-well plate at a concentration of 10^5 colony forming units (CFU)/mL and incubated with 100 μL of DPPLM NPs at serial concentrations from 0 to 100 μg/mL at 37 °C for 24 h. The OD value of the suspensions in each well was measured using a TECAN microplate reader at 600 nm at defined time points. The minimum inhibitory concentration (MIC) was taken as the lowest concentration at which the well was clear. After spreading these test dilutions for MIC determination on agar, the minimum bactericidal concentration (MBC) was

determined as the lowest concentration that yielded no bacterial colonies on the plate.

A bacterial suspension at a concentration of 10^5 CFU/mL was added to a 6-well plate covered with sterile square slides and incubated at 37 °C for 24 h under stationary conditions. Thereafter, the medium was removed and the bacterial pellets were rinsed with PBS three times. DPPLM NPs (2 mL) at a concentration of 200 μg/mL were added carefully to the wells. The plate was cultured for another 24 h. Thereafter, the bacterial pellets were rinsed with PBS three times and fixed with 4% (v/v) paraformaldehyde sputter-coated with gold. Finally, the morphological changes to the bacteria were observed using scanning electron microscopy (SEM).

2.16. Live/dead biofilm staining

The bacterial suspension was added to a 24-well plate at the concentration of 10^5 CFU/mL and incubated for 24 h. Thereafter, the bacterial suspension was discarded, and the wells were washed with PBS three times to remove planktonic bacteria. DPPLM NPs were added and incubated for 12 h. Bacteria were stained with a L7007 LIVE/DEAD BacLight Staining Kit (Thermo Fisher Scientific) for 15 min in the dark at room temperature. All bacteria were stained with SYTO9 to produce green fluorescence, and dead bacteria with damaged membranes were stained with propidium iodide to produce red fluorescence. A fluorescence microscope was used to capture the images of each sample.

2.17. Establishment of the DM rat model

Preparation of the High-Fat Diet (HFD)/STZ-Induced Diabetic Rats: Male Sprague Dawley (SD) rats (200–250 g) were purchased from Experimental Animal Center of Chongqing Medical University. To establish a type 2 diabetic (T2DM) rat model, rats were fed with HFD (60% fat; Research Diets, D12492) for 2 weeks. After consumption of HFD for 2 weeks, rats were injected intraperitoneally with STZ dissolved in sodium citrate buffer (pH 4.5, prepared immediately before use) at a dose of 35 mg/kg. The rats' blood glucose levels were measured every week using a Roche glucose meter, and the rats with ≥16.7 mmol/L random blood glucose levels were considered diabetic and offered HFD till the end of the study. An oral glucose tolerance test (OGTT) was performed to confirm the successful establishment of the diabetic rat model. Briefly, rats were fasted for 12 h and then received an intragastric administration of glucose (2 g/kg). Their blood glucose was tested at defined time points. The animal handling and surgical procedures were conducted in accordance with protocols approved by the Research Ethics Committee of the Stomatological Hospital of Chongqing Medical University (CQHS-REC-2021 (LSNo. 28)).

2.18. Establishment of experimental periodontitis model in diabetic rats (DMEP) and animal treatments

DM rats were used to establish an experimental periodontitis (EP) model. Briefly, DM rats were anesthetized with intraperitoneal injections of 10% chloral hydrate (20 mg/kg of body weight), and then a ligature wire with a diameter of 0.2 mm was placed around the maxillary first molars for 2 weeks. Subsequently, before surgery, the collagen membrane (CM) was sterilized in UV for 20 min and immersed in 1000 μg/mL DPPLM solution or a mixture of 136 μg/mL ALA and 172 μg/mL Mino (free drug) for 30 min. Twenty-four diabetic rats with periodontitis (DMEP rats) were randomly divided into four groups (n = 6 per group), and the CMs were placed into the interproximate space between the maxillary first molars and the maxillary secondary molars: (1) Untreated group (diabetic periodontitis rats without treatment), (2) CM group, (3) CM + free drug group, (4) CM + DPPLM group. Animals were sacrificed after 2 weeks and their maxillaries were collected, fixed in 4% paraformaldehyde for 2 days, and then rinsed with PBS for further analyses. Microcomputed tomography (micro-CT) analysis was used to examine

the amounts of bone loss. The vertical bone loss was determined by measuring the distance between cemento-enamel junction (CEJ) of the maxillary molars and the alveolar bone crest (ABC). After micro-CT, the samples were decalcified in 10% EDTA for 4 weeks, dehydrated in gradient alcohol, embedded in paraffin, and sectioned at 5 μm thickness for hematoxylin and eosin (H&E) staining and Masson's staining. The morphological characteristics of bone healing were observed under a light microscope (IX71–400X, OLYMPUS, Tokyo, Japan).

2.19. In vivo antibacterial testing of DPPLM NPs

The tooth was carefully extracted from the alveolar bone and the plaque biofilms covering the tooth surface were observed using SEM.

Standard plate counting: The dental plaque was collected from the tooth surface using a cotton swab, which was soaked in sterile deionized water, and then ultrasonically shaken to obtain a bacterial suspension. The bacterial suspension was then diluted by 10-fold and 100 μL of the dilution was plated on LB agar and cultured at 37 °C for 24 h.

2.20. Statistical analysis

All experimental data are presented as the mean ± standard deviation (SD), and the results were analyzed using one-way analysis of variance (ANOVA) or two-way ANOVA analysis among three or more groups followed by Tukey's *post hoc* test. A value of $P < 0.05$ was considered statistically significant (*$P < 0.05$, **$P < 0.01$, ***$P < 0.001$, ****$P < 0.0001$). At least three independent experiments were performed in this study.

3. Results

3.1. Design, preparation, and characterization of DPPLM NPs

DSPE-PEG-NHS was self-assembled in water, and then covalently linked to the amino group on the surface of PAMAM by an amidation reaction between succinic anhydride and the amino-ended PAMAM at different molar ratios (76.8: 1, 32:1, 6.4:1) to obtain the amphiphilic copolymer, named DSPE-PEG-PAMAM (DPP) (Fig. 1A, Figs. S2 and S3).
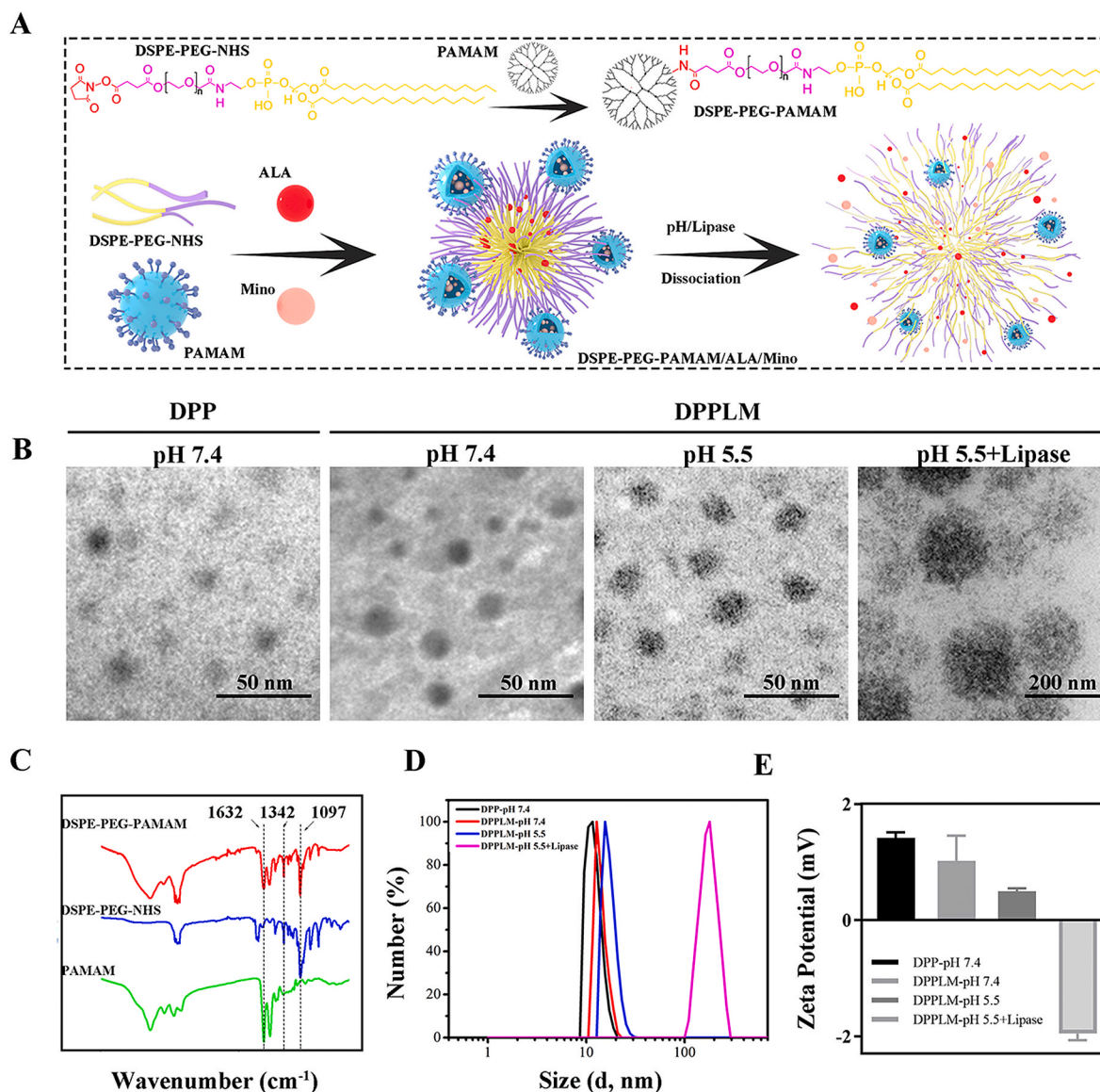

Fig. 1. Preparation and characterization of DPPLM NPs. Schematic illustration and preparation of DPPLM (A). TEM images (B) of blank DSPE-PEG-PAMAM (DPP), DPPLM at PH 7.4, DPPLM at PH 5.5 and DPPLM at PH 5.5+Lipase. FTIR spectra (C) of PAMAM, DSPE-PEG-NHS, and DSPE-PEG-PAMAM. DLS (D) and zeta potential (E) of DPP, and DPPLM at pH 7.4 or 5.5 buffers in the absence or presence of lipase. The results are presented as the means ± standard deviation (SD).

When the molar ratio of DSPE-PEG and PAMAM was 6.4:1, DPP NPs had a relatively high drug loading content, because the drug loading content increased as the content of PAMAM increased, while there were no significant differences in the size and surface charge of the three kinds of DPP NPs. Therefore, the composition of DSPE-PEG and PAMAM in DPP NPs was fixed at 6.4:1 for subsequent experiments.

As shown in the ^{1}H NMR spectrum (Fig. S1), the characteristic peaks of PAMAM appeared in the spectra at 2.42, 2.62, 2.72, 2.81, 3.23, and 3.28 ppm, corresponding to H6–H1. The characteristic peaks of PEG (–CH$_2$O–) and DSPE (–CH$_2$–) were detected at 3.69 ppm and 1.29 ppm, respectively. After conjugation, the spectrum of DPP exhibited characteristic chemical shifts of hydrogens in DSPE-PEG and PAMAM, which confirmed that PAMAM was successfully introduced into the DSPE-PEG-NHS molecules. According to the peak area of DSPE-PEG and PAMAM, the molar ratio of DSPE-PEG and PAMAM in the product was approximately 4. The FTIR spectra of the raw materials are presented in Fig. 1C. PAMAM presented characteristic peaks of amide I and amide II at 1632 cm^{-1} and 1543 cm^{-1}, respectively. The characteristic peaks of PAMAM at 3074 cm^{-1} and 3276 cm^{-1} corresponded to the strong vibration of *N*–H in the peripheral amino group. The peaks at 2830 cm^{-1} and 2934 cm^{-1} were attributed to C–H stretching. For DSPE-PEG-NHS, the characteristic peaks located at 1097 cm^{-1} were attributed to C–*O*–C stretching vibrations, the absorption peaks corresponding to 1342 cm^{-1} belonged to C–H wagging vibration. After the conjugation reaction between DSPE-PEG-NHS and PAMAM, the characteristic peaks for νC-*O*-C (1097 cm^{-1}), ωC-H (1342 cm^{-1}) of DSPE-PEG, and νC-O (1632 cm^{-1}) of PAMAM were clearly shown in the FTIR spectrum of DSPE-PEG-PAMAM. These results suggested that PAMAM was successfully conjugated to DSPE-PEG.

Then, ALA-loaded DSPE-PEG NPs were prepared using the nanoprecipitation method, and Mino-loaded PAMAM was synthesized via electrostatic interaction. To optimize the drug loading content (DLC) and drug loading efficiency (DLE), we further investigated the drug-loaded NPs by varying the weight ratios of polymeric DPP/drug. The DLC of ALA increased from 7% to 16.83% and the DLE declined from 53.72% to 34.71% when the drug to DSPE-PEG (DP) ratio increased from 2:15 to 8:15. The DLC and DLE of ALA used in this study was 13.61% and 51.88%, respectively. Furthermore, ALA and Mino were co-encapsulated into micelles, and the maximal DLC of Mino that could be achieved was 17.17%, and the DLE of Mino was 33.37% in this study (Table 1).

We also measured the zeta potential of DPP and DPPLM NPs. DSPE-PEG NPs presented negatively charged zeta potentials (-2.02 ± 0.61 mV) (Fig. S3). However, the zeta potential was neutral or positive after the conjugation with PAMAM, and the zeta potential of DPPLM NPs was 1.02 ± 0.35 mV (Fig. 1E), making NPs more likely to adhere to negatively charged bacteria via electrostatic interactions. TEM imaging (Fig. 1B) indicated that the morphology of both blank DPP and DPPLM NPs was irregular spheres. DLS analysis (Fig. 1D) revealed that the size of DPPLM NPs was approximately 12.78 nm, which was slightly larger than the blank DPP NPs (approximately 11.58 nm).

3.2. Drug release from DPPLM NPs was enhanced in an acidic and lipase-containing environment

Meanwhile, we addressed the NPs' response to pH and bacterial enzymes using TEM and DLS *in vitro* (Fig. 1B, D). The DLS results

Table 1
Drug loading content (DLC) and drug loading efficiency (DLE).

	DLC of Mino	DLE of Mino	DLC of ALA	DLE of ALA
DPPL$_4$	-	-	7%	53.72%
DPPL$_8$	-	-	13.61%	51.88%
DPPL$_{16}$	-	-	16.83%	34.71%
DPPL$_8$M$_{16}$	17.17%	33.37%	-	-

Table 2
The primer sequences of all genes used in qPCR.

Gene	Forward primer (5′~3′)	Reverse primer (5′~3′)
Gapdh	CAAGTTCAACGGCACAGTCA	CCATTTGATGTTAGCGGGAT
Alp	AGATGTGGCGGTCTTTGC	TCAGAACAGGGTGCGTAGG
Ocn	CTCACTCTGCTGGCCCTGAC	CCTTACTGCCCTCCTGCTTG
Opn	AGAAACGGATGACTTTAAGCAAGAA	TCTCTGCATGGTCTCCATCGT
Runx2	CGGGAACCAAGAAGGCACA	AGGCGGGACACCTACTCTCATA
Osx	GCCTACTTACCCGTCTGACTTTG	TGCCCACTATTGCCAACTGC

indicated that the DPPLM NPs swelled slightly (approximately 15.54 nm) at pH 5.5. When the NPs were incubated at pH 5.5 with lipase, the DLS results showed a significant increase to 180 nm in diameter, which might be ascribed to the disassembly and re-agglomeration of the NPs. The results were consistent with the morphological changes of NPs observed by TEM. We also measured the zeta potential (Fig. 1E) of DPPLM NPs at pH 5.5, with or without the lipase, which showed that when DPPLM NPs were incubated with the lipase, their zeta potential was reduced to -1.95 ± 0.10 mV, which was similar to that of DSPE-PEG (Fig. S3). The size changes revealed that the DPPLM NPs facilitated the on-demand release of drug in the acidic microenvironment and in the presence of lipase.

Next, we investigated the accumulated release of ALA and Mino from DPPLM NPs in response to pH or in the presence of lipase, respectively. Fig. 2A shows that in the presence of lipase, DPPLM NPs exhibited an enhanced release behavior of ALA compared to that without enzymes, which was ascribed to the catalyzed degradation of the DSPE-PEG cores and the resultant disintegration of the DPPLM NPs. As shown in Fig. 2B, the release of Mino at pH 5.5 was a little faster than that at pH 7.4, which could be attributed to the weakened electrostatic interactions between Mino and PAMAM under acidic conditions. In summary, these results indicated that the acid and lipase promoted drug release feature will endow the system with a preferential drug release profile.

We also determined the penetration and retention of PAMAM into hard tissue. As shown in Fig. S5A, the fluorescent signal was visible at the cortical layer of the bone along the direction of diffusion at 5 days after administration, indicating that PAMAM-FITC was able to penetrate into the superficial layer of bone. Furthermore, the penetration of PAMAM into the root was determined using confocal microscopy and fluorescence microscopy. Figs. S5B and C shows fluorescence signals in the cementum layer of the root, which demonstrated that PAMAM could penetrate slightly into the cementum. Collectively, these results indicated that the small-sized PAMAM NPs were possibly able to penetrate into the hard tissue to deliver the drugs to a certain extent.

3.3. DPPLM NPs had good biocompatibility and were effectively endocytosed by BMSCs

The cytotoxicity of drug-loaded nanoparticles against BMSCs were measured using a CCK8 assay. The results indicated that DPPLM NPs showed low cytotoxicity after incubation for 24 h, even at relatively high doses (Fig. 2C).

To investigate cellular uptake behavior of NPs, we labeled DPP NPs with FITC. Meanwhile, Nile red, a hydrophobic fluorescent dye, and Rhodamine B, a hydrophilic fluorescent dye, were encapsulated in FITC-labeled NPs as model drug substitutes for ALA and Mino, respectively. The cellular uptake of DPP-FITC NPs in BMSCs was confirmed using flow cytometry (Fig. 2D). Furthermore, CLSM images (Fig. 2E and F) showed that the intensity of red and green fluorescence in the BMSCs increased gradually from 2 to 24 h after incubation with fluorescently-labeled NPs, which indicated the successfully internalization of NPs by cells.

Furthermore, we investigated the subcellular localization of NPs in BMSCs using CLSM (Fig. 2G). The lysosomes were labeled by Lyso-Tracker Green. The red fluorescence was very weak at an incubation time of 20 min, indicating that few NPs were absorbed into cells at this
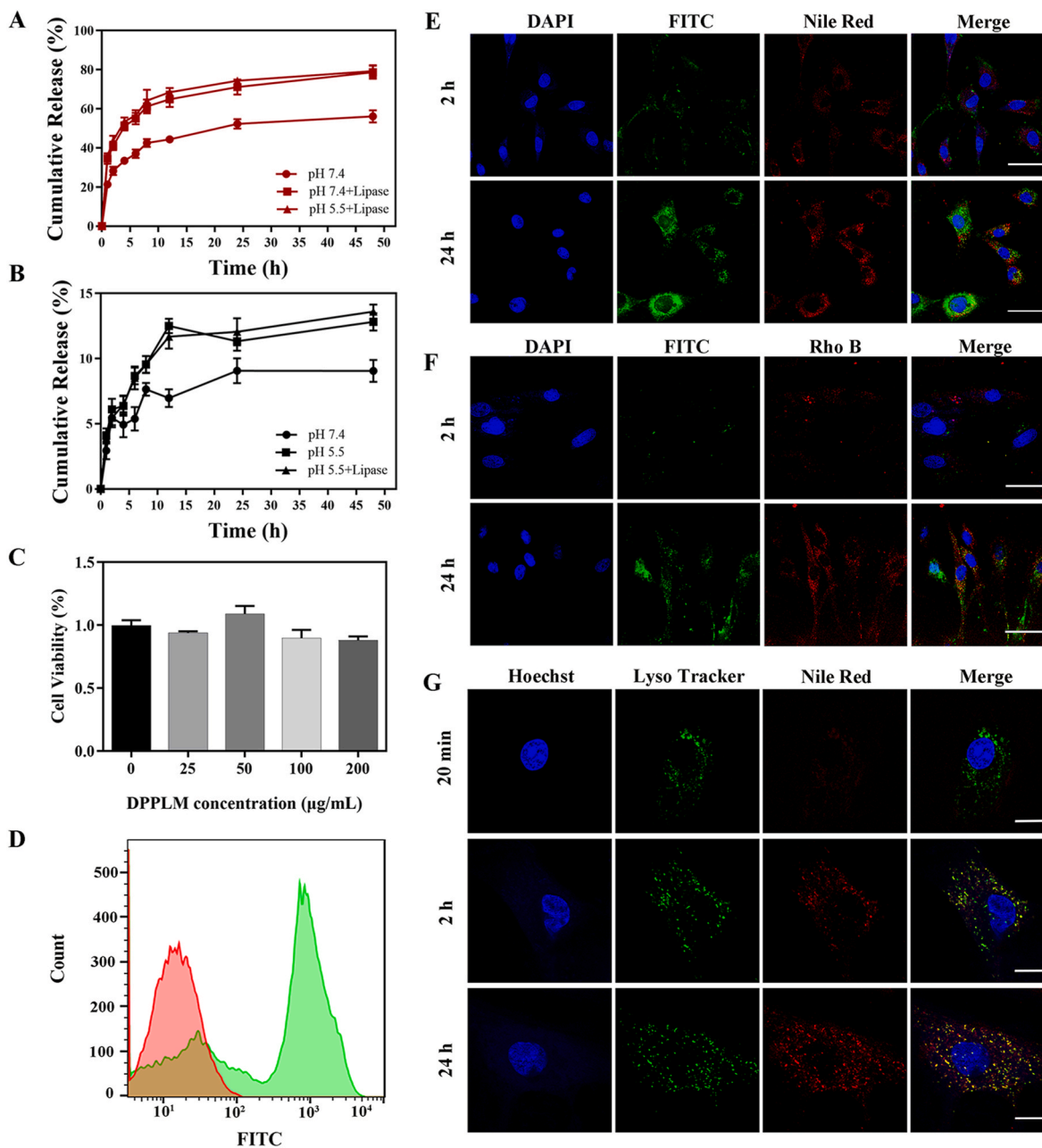
Fig. 2. Drug release profile, cell viability, cell uptake, and subcellular localization of DPPLM NPs. *In vitro* ALA (A) and Mino (B) release from DPPLM in different buffers. The *in vitro* cytotoxicity (C) against BMSCs after incubation with DPPLM for 24 h at different concentrations. Flow cytometry (D) of the cellular uptake in BMSCs after incubation with 10 μg/mL DPP-FITC NPs for 24 h, Red: PBS, Green: DPP-FITC NPs. (E) The cellular uptake of Nile red dye and FITC-labeled DPP (DPP-FITC/Nile red) NPs at different time points, scale bars: 50 μm. (F) The cellular uptake of Rhodamine B (Rho B) and FITC-labeled DPP (DPP-FITC/Rho B) NPs at different time points, scale bars: 50 μm. CLSM images (G) of BMSCs incubated with 10 μg/mL Nile red-loaded DPP (DPP/Nile red) NPs at different time points, scale bars: 10 μm. The results are presented as the means ± SD. Nile red dye and Rhodamine B were used as substitutes for ALA and Mino, respectively. The nuclei were stained blue with DAPI and Hoechst.

time. After 2 h of incubation, a large amount of yellow staining (the overlap of red and green fluorescence) was observed, suggesting that endocytosed NPs were mainly transported through the endolysosomal pathway. At 24 h, some red fluorescence was also observed in the cytoplasm, which demonstrated that the drug might successfully escape from the lysosomes into the cytoplasm because of the proton sponge effect of the NPs [38]. Taken together, these results demonstrated that the drug-loading nanocarrier system could be effectively endocytosed by BMSCs and the loaded drugs were subsequently released.

3.4. DPPLM NPs relieved AGE-suppressed osteogenic differentiation of BMSCs and alleviated AGE-induced ROS production and inflammation in vitro

A large amount of evidence suggests that increased production of AGE, which are the products of nonenzymatic glycation of macromolecules (proteins, lipids, and nucleic acids) accumulates in bone tissue during DM [9]. Thus, we further established a model to mimic the diabetic environment using AGE-BSA *in vitro*, which is modified by a variety of AGE structures and resembles *in vivo* generated forms.

First, we verified that ALA had a good ability to promote osteogenic

differentiation of BMSCs using Alizarin Red staining and quantitative analysis. The results shown in Fig. 3A and B indicated that ALA-treated BMSCs had over two-fold more calcium deposition and mineralization nodules than did the control group. Then, we investigated the osteoinductive properties of DPPLM NPs. As shown in Fig. 3C and D, the DPPLM group promoted the formation of mineralized nodules significantly, while the negative effect of AGE-BSA on the osteogenic differentiation of BMSCs was reversed in the AGE + DPPLM group. Additionally, qRT-PCR (Fig. 3E–I) revealed that the mRNA expression of osteogenic genes [*Alp* (alkaline phosphatase), *Opn* (osteopontin), *Osx* (osterix), *Ocn* (osteocalcin), and *Runx2* (runt-related transcription factor 2)] were downregulated in the AGE-BSA group, but recovered in the AGE + DPPLM

group after incubation for 7 days, indicating that treatment with DPPLM NPs enhanced the osteogenic differentiation and mineralization of BMSCs in a diabetic pathological environment.

To determine the underlying mechanisms of DPPLM *N*P-mediated osteogenesis, we subsequently examined the intracellular ROS and iNOS levels. As shown in Fig. 3J, the AGE group presented increased numbers of positive cells compared with those in the other groups. However, marked suppression of ROS generation was detected in the DPPLM + AGE and DPPLM groups. The immunofluorescence staining data showed that the expression of iNOS in AGE-induced BMSCs was markedly enhanced, while the expression of iNOS in DPPLM + AGE group was reduced (Fig. 3K), which showed a similar trend to the intracellular ROS
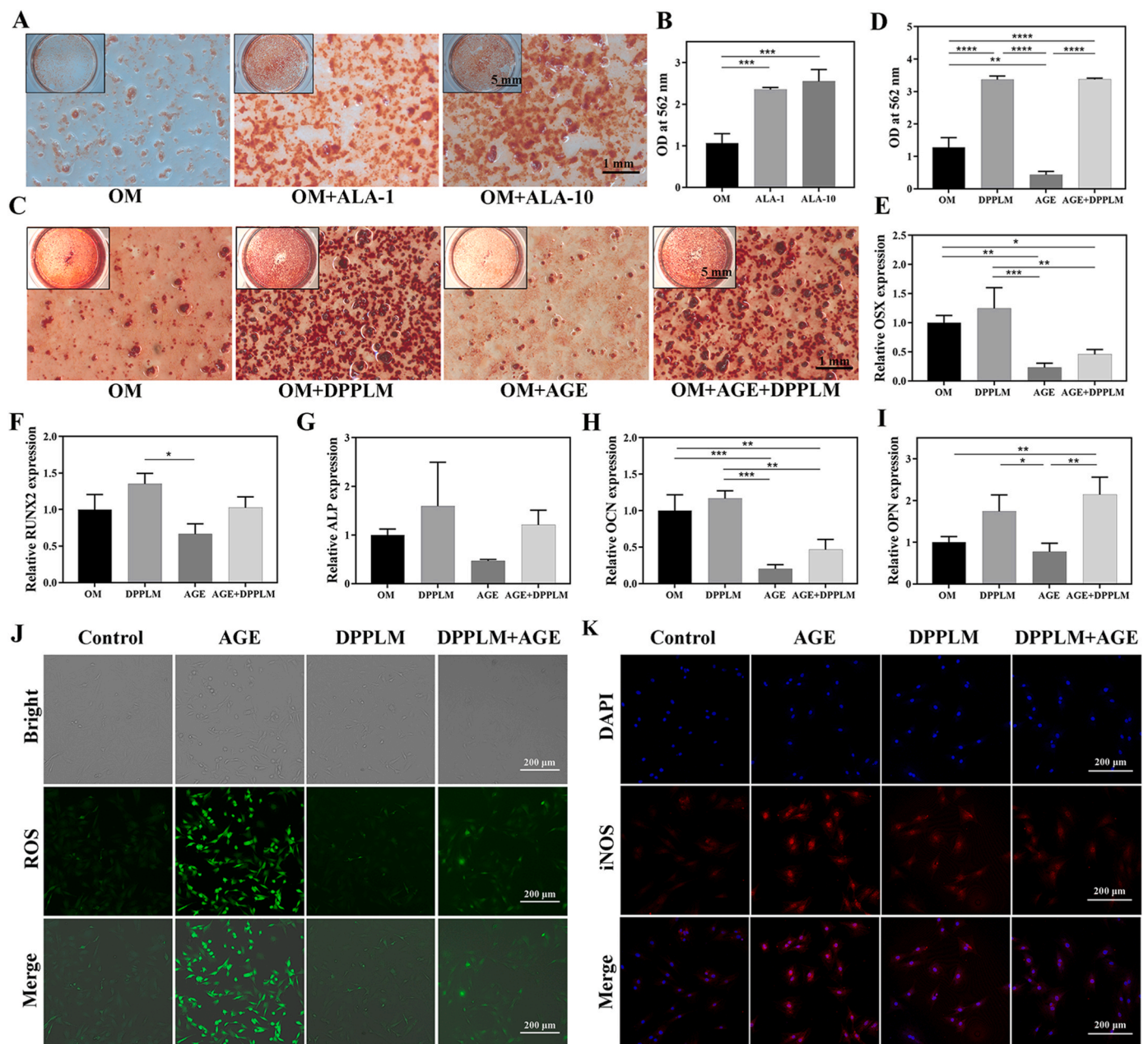

Fig. 3. Osteogenic, antioxidative and anti-inflammatory effects of DPPLM NPs *in vitro*. BMSCs were cultured with different treatments under osteogenic induction medium (OM). Alizarin-Red staining (A) of calcium nodules and quantification of calcium deposition (B) of cells treated with PBS, 1 μg/mL ALA, and 10 μg/mL ALA at day 14 after culture. Alizarin-Red staining (C) and quantification of calcium deposition (D) of BMSCs treated with PBS, 100 μg/mL AGE, 100 μg/mL DPPLM NPs, and 100 μg/mL DPPLM mixed with 100 μg/mL AGE at day 14 after culture. Osteogenic gene expression of *Osx* (E), *Runx2* (F), *Alp* (G), *Ocn* (H), and *Opn* (I) of BMSCs with different treatments after culturing for 7 days measured using qRT-PCR. Typical *in vitro* fluorescence images of ROS formation (J) and iNOS (K) of BMSCs exposed to PBS, AGE, DPPLM, or AGE + DPPLM. Data are presented as means ± SD, *P < 0.05, **P < 0.01, ***P < 0.001, and ****P < 0.0001; by one way analysis of variance (ANOVA) with Tukey's *post hoc* test (B, D, E, F, G, H, I).

changes. In summary, the results indicated that the novel nanocarriers, DPPLM NPs, could inhibit inflammatory processes by reducing the overproduction of ROS and attenuating the level of iNOS, which might contribute to the enhanced osteogenic differentiation ability.

3.5. DPPLM NPs exhibited antibacterial properties in vitro

We selected *E. coli* (a typical gram-negative bacteria) and *S. aureus* (a typical gram-positive bacteria) to evaluate the antibacterial activity of the DPPLM NPs. The broth microdilution method was used to evaluate the minimum inhibitory concentration (MIC) and minimum bactericidal concentration (MBC) of the DPPLM NPs. The MIC value of DPPLM was
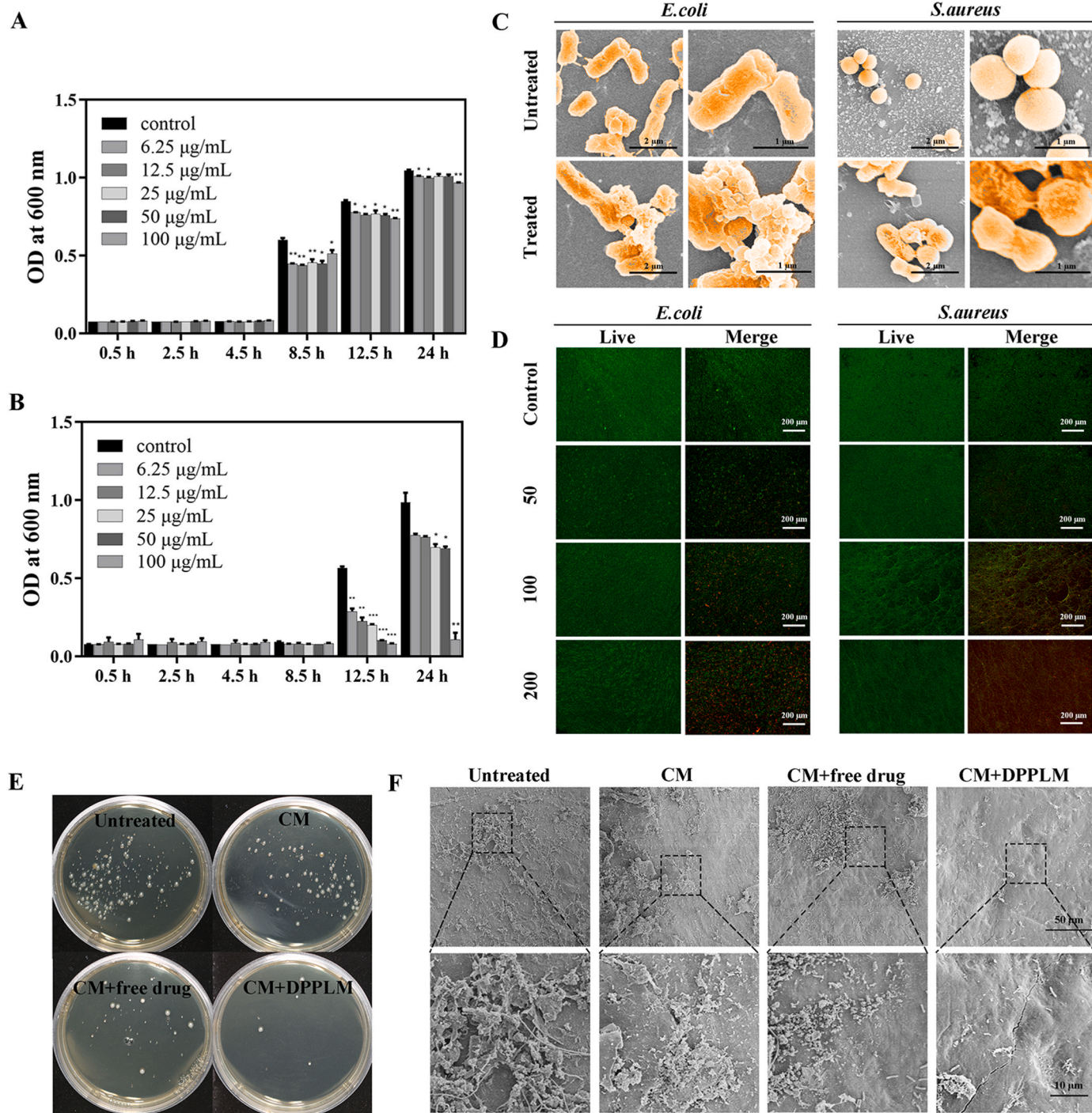

Fig. 4. Antibacterial activity of DPPLM NPs *in vitro* and *in vivo*. Viability of *E. coli* (A) and *S. aureus* (B) after incubation for 24 h for different time periods at different DPPLM concentrations. (C) Typical SEM images of *E. coli* and *S. aureus* after treatment for 24 h with 200 μg/mL DPPLM using PBS treatment as a control. (D) Fluorescence microscopy images of *E. coli* and *S. aureus* after incubation for 12 h with 0, 50, 100, and 200 μg/mL DPPLM, Green: live bacteria, Red: dead bacteria. (E) Digital photographs of bacterial colony-forming units, obtained from the tooth surface treated under different experimental conditions. (F) SEM images on the surface of the rat teeth under different experimental conditions. All data are presented as the means ± SD. *$P < 0.05$, **$P < 0.01$, ***$P < 0.001$, compared with the control group; by two-way analysis of variance (ANOVA) with Tukey's *post hoc* test (A, B).

100 µg/mL against *S. aureus*, which was lower than that against *E. coli* (300 µg/mL), probably because *S. aureus* is highly sensitive to Mino. The MBC values of DPPLM against *S. aureus* and *E. coli* were 400 µg/mL and 800 µg/mL, respectively. Next, the dynamic antibacterial activity of DPPLM was monitored on the basis of the optical densities (OD values) of bacterial suspensions incubated with different concentrations of DPPLM over 24 h. Fig. 4A and B shows that the DPPLM NPs exhibited dose-dependent inhibition of the growth of *S. aureus* and *E. coli*, and the OD values of *S. aureus* showed a sharp reduction at a concentration of 100 µg/mL, while the result of *E. coli* showed a slower declining trend. The morphological changes to *E. coli* and *S. aureus* were observed using SEM after treatment with DPPLM NPs (Fig. 4C). The control group exposed to PBS had relatively smooth surfaces with intact membrane structures, while the DPPLM group exhibited distorted and corrugated surfaces, and the bacterial cell membrane was ruptured and shrunk

significantly. Bacterial live/dead fluorescence staining was used to identify the antibacterial effects of DPPLM NPs toward *E. coli* and *S. aureus*. Live bacteria could be highlighted in green (SYTO9) and dead bacteria could be visualized in red (propidium iodide). The results showed that the control group comprised predominantly live bacteria. After treatment with DPPLM NPs, the number of dead or compromised bacteria gradually increased with the increasing concentration of NPs, corresponding to the increase of red fluorescence in the *E. coli* or *S. aureus* cultures (Fig. 4D). Taken together, the DPPLM NPs demonstrated an effective bactericidal capability, which could be ascribed to their small size, positive surface charge, and high loading efficiency of Mino.
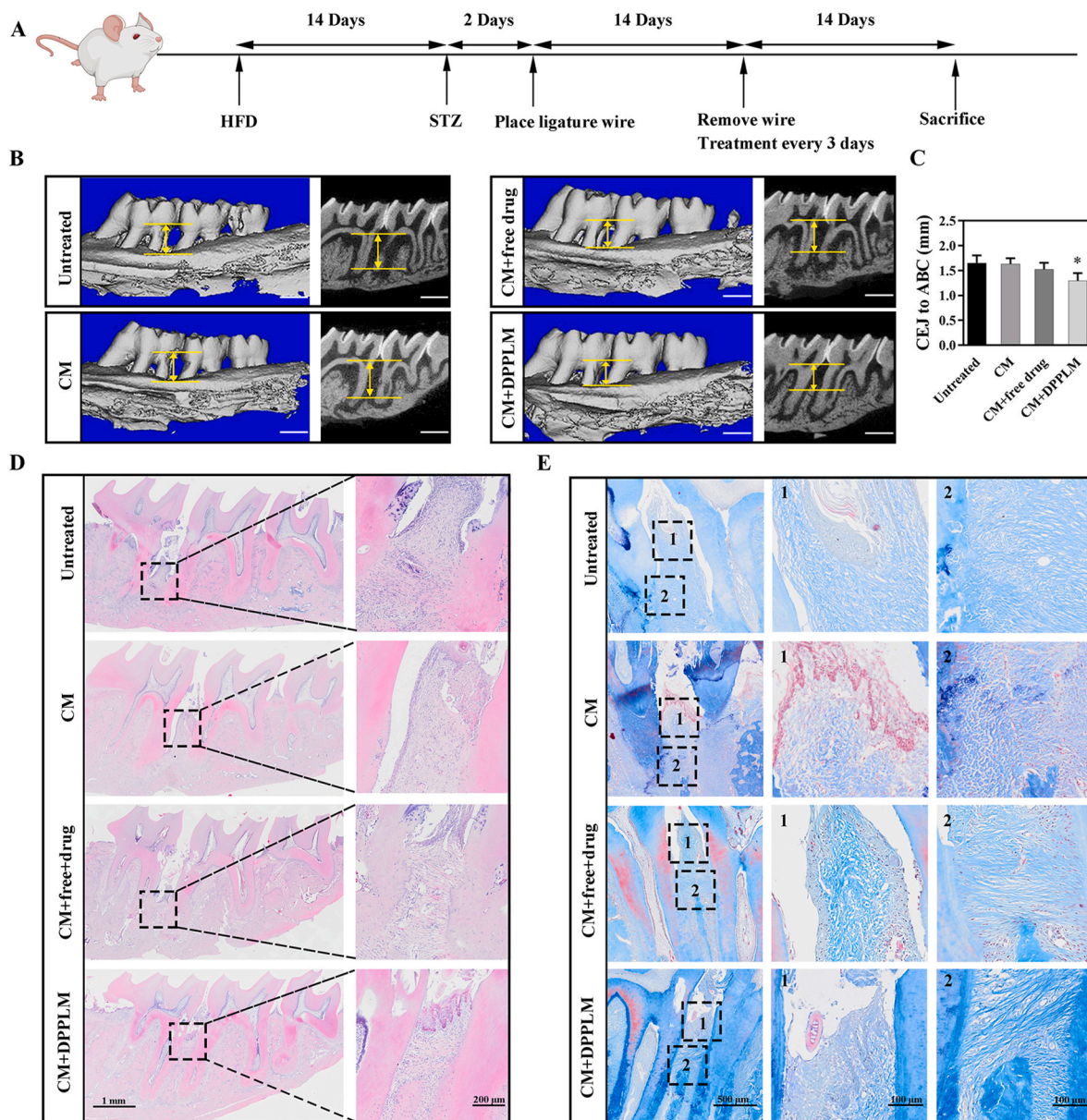

Fig. 5. *In vivo* **ability of DPPLM NPs to ameliorate periodontal bone loss under DM conditions.** (A) Treatment schedule. (B) Micro-CT images of maxillary alveolar bone at the palatal side, treated under different experimental conditions. The images with a black background are representative sagittal micro-CT slices; the images with a blue background are three-dimensional micro-CT reconstruction images. Scale bar: 1 mm. (C) Quantitative analysis of the distance between CEJ and ABC. Data are presented as means ± SD, *$P < 0.05$, compared with the untreated group; by one way analysis of variance (ANOVA) with Tukey's *post hoc* test. H&E staining images (D) and (E) Masson's staining of the periodontium treated under different experimental conditions.

3.6. DPPLM NPs reduced periodontal pathogens in DM rats

A rat experimental periodontitis model of type 2 diabetes mellitus (T2DM) was established to evaluate the antibacterial ability of DPPLM NPs and their periodontal regeneration ability *in vivo* (Fig. 5A). An oral glucose tolerance test (OGTT) was performed to confirm that the T2DM rat model was successfully established [47]. Fig. S6 shows that the blood glucose levels in both DM and control groups increased during the initial 30 min and gradually decreased over the following 120 min, whereas the sustained high glucose level in the DM group suggested the successful establishment of hyperglycemia. When the blood glucose of the rats was over 16.7 mmol/L, we created the experimental periodontitis model in these rats and then carried out the experiments.

To evaluate the antibacterial effect *in vivo*, we performed plate counting methods and SEM. We counted the bacterial colonies originally derived from the teeth surface (Fig. 4E). Only a few bacterial colonies were seen in CM + DPPLM group, which was less than in the CM + free drug group, while there were a large amount of bacteria in the Untreated group and CM group (Fig. 4E). These results indicated that the antibacterial effect of the CM + DPPLM group was better than that of the CM + free drug group, and much better than that of the Untreated group and CM group. Next, we observed the morphology of the dental plaque that was attached to the surfaces of the teeth after DPPLM treatment using SEM. Fig. 4F shows that a large amount of bacteria were closely packed and interlaced as a plaque biofilm in the Untreated group, which was similar to the images exhibited in CM group. Small amounts of bacteria were scattered in the CM + DPPLM group, indicating that the DPPLM NPs had a more effective antibacterial activity.

3.7. DPPLM NPs alleviated periodontal bone loss in DM rats

To investigate the osteogenesis of DPPLM NPs under DM conditions *in vivo*, micro-CT was conducted and the distance between the CEJ-ABC on the palatal side of the first maxillary molar was measured. To ensure the consistency of the measurement standards, we viewed the micro-CT reconstructed images from the same angle and adjusted all tooth cusps on the same plane. No significant difference in the vertical distance between the CEJ-ABC was found in the DM group and in the healthy group, while the CEJ-ABC distance in the periodontitis group increased, and the CEJ-ABC distance in the diabetic periodontitis group was significantly enhanced compared with that of the healthy group (Figs. S7 and S8). These results indicated that the diabetic periodontitis model was successfully established, and that DM led to the increased alveolar bone loss. As shown in Fig. 5B and C, the collagen membrane (CM) group showed no bone healing effects, the CEJ-ABC distance of which was equal to the Untreated group, indicating that the CM had no influence on bone regeneration. The CEJ-ABC distance of the CM + free drug group showed a slight reduction; however, the difference was not statistically significant compared with that of the Untreated group, indicating that the free drug insufficiently promoted osteogenesis. The CEJ-ABC distance in the CM + DPPLM group was significantly reduced, by an average of 0.357 mm, compared with that of the Untreated group, indicating a positive effect of DPPLM on delaying alveolar bone loss.

To further evaluate the inflammatory status and periodontium regeneration, we performed H&E staining and Masson's staining of the alveolar bone. We observed unattached and more disordered periodontal ligaments between the maxillary first molars and maxillary second molars in the Untreated group, CM group, and CM + free drug group, while the ligaments in the DPPLM group were denser and well arranged (Fig. 5D and E). In addition, the DPPLM group showed a shorter CEJ-ABC distance, which indicated that DPPLM could inhibit periodontal destruction. In summary, the results indicated that the DPPLM NPs effectively inhibited periodontal bone loss.

4. Discussion

Advanced nanoscale systems of a distinct nature have exhibited promising prospects by taking advantage of special microenvironmental changes to achieve controlled drug release for bone regeneration. Efforts to produce superior nanoscale systems are ongoing. In particular, a great deal of research has been carried out on stimuli-responsive nanoscale systems for drug delivery to ensure the therapeutic effect of their cargoes at the site of infection. In the present study, a pH/lipase-responsive dual-drug delivery system was designed to exert antibacterial, antioxidant, anti-inflammatory, and osteoinductive functions in diabetic microenvironments to inhibit alveolar bone loss under DM conditions.

It has been reported that the biofilm microenvironment is relatively acidic (pH 4.5–6.5) because of anaerobic fermentation [31]. Some molecules and groups can be protonated under acidic conditions and are deprotonated under alkaline conditions. Thus, their hydrophilicity will undergo a sharp reversal to change the structure and morphology of their assemblies [25]. Several studies have demonstrated that PAMAM-based nanocarriers can be developed to respond to pH changes, attributed to the conformational changes from a "dense core" at high pH to a "dense shell" at low pH [32]. In the present study, the PAMAM-based nanocarrier system responded to pH and accelerated the release of the transported drug (Fig. 2A and B). Moreover, at the cellular level, because of the proton sponge effect of PAMAM, the acidic microenvironment could promote the escape of the nanocarriers from the lysosomes into the cytoplasm, which was confirmed by subcellular localization experiments (Fig. 2G). In addition, the PAMAM nano-architectures designed in the present study could improve drug solubility and drug permeation. It is well documented that some specific enzymes (e.g., esterase, lipase, and gelatinase) are overexpressed in biofilm-associated infections [29,42], and can be exploited to achieve enzyme-mediated drug release. In this work, the incorporation of DSPE-PEG not only introduced the capability to respond to lipase, but also improved the pharmacokinetics of PAMAMs, reduced their toxicity, and increased the solubility and enhanced the bioavailability of hydrophobic drugs. Overall, the DPPLM NPs incorporated the positive attributes of PAMAM and DSPE-PEG to overcome the disadvantages of current drug delivery systems and simultaneously incorporated the benefits of both carrier systems. The hydrophilic blocks of PAMAM formed the outer shell, which protected Mino from direct damage by the outside environment, such as hydrolysis and enzymatic degradation, to enhance its stability and prolong its circulation time in the body. The hydrophobic blocks of DSPE-PEG constituted the inner core and encapsulated the poorly soluble drug, ALA, which improved the drug's solubility and stability.

According to the results of TEM, DLS, and zeta potential analysis, the DPPLM NPs were small in size and positively charged. Size and charge can influence the penetration behavior of nanoparticles in biofilms. Gao and co-workers reported that azithromycin (AZM)-conjugated clustered nanoparticles (denoted as AZM-DA NPs) with a small size and positive surface charge exhibited excellent penetration and retention capability inside biofilms, both *in vitro* and *in vivo* [31]. Notably, small-sized NPs are particularly beneficial for drug delivery because they can reduce diffusional hindrance, accumulate and penetrate deeper into the inner regions [48]. Similarly, in our study, the small size and positive surface charge endowed the DPPLM NPs with the ability of penetration and retention in local infected tissue. In addition, the bacterial membrane is generally negatively charged [31]. Thus, the positive surface charge of DPPLM promoted interactions with the negatively charged bacterial wall, and led to increased nanoparticle uptake in both Gram-positive and Gram-negative bacteria.

Previous studies have demonstrated that DM increases the risk of periodontitis for the reason of increased AGE deposition, increased ROS production, and subsequently exaggerated inflammation in the periodontal tissues. It is widely known that ROS produced by immune cells have antibacterial effects [49,50] by reacting with their essential

macromolecules such as DNA, RNA, and pathogenic proteins, damaging the cell membrane and cell wall and causing the pathogen's death [51]. However, the relatively sudden release of ROS produced by immune cells has become known as the "oxidative burst" [52,53] or "respiratory burst" [54]. While a transient burst of ROS is important for the elimination of pathogens, overproduction of ROS that overwhelms the antioxidant defense system will lead to oxidative stress, interfere with cell cycle progression, and impair osteogenesis [55], which might be more pernicious for periodontal bone regeneration. Therefore, the reduction of ROS overproduction and inflammation, along with the promotion of osteogenic differentiation, are beneficial for periodontal bone regeneration under DM conditions. Hence, transporting a feasible therapeutic agent to periodontal tissues is of great significance to achieve this ambitious goal. ALA, a natural ingredient of the human body, not only acts as a powerful antioxidant, but also displays anti-inflammatory, immunomodulatory, and osteoinductive effects [46,56,57]. We confirmed that ALA promotes osteogenic differentiation of BMSCs using Alizarin Red staining (Fig. 3A). Moreover, ALA has emerging roles in the prevention of diabetes complications and bone loss, as well as in the inhibition of periapical bone loss [46,56,58]. Therefore, we choose ALA as one of the model drugs for the treatment of diabetic periodontitis. Although ALA cannot be applied locally because of its poor aqueous dispersibility, difficulty in permeating into periodontal tissue, possible side effect, the drug-loaded nanoparticles effectively solved these problems. In our study, ALA was encapsulated in the inner core of the hydrophobic blocks of DSPE-PEG using the nanoprecipitation method and was released responsively from the nanosystem under lipase conditions (Fig. 2A).

Moreover, prolonged exposure to ROS in DM will be beneficial for bacteria and can induce protective functions [49], resulting in opportunistic pathogens being retained and accumulating over time. Periodontitis treatment under a DM environment also requires antibiotics to control bacterial infections. In this work, DPP NPs showed no antibacterial activity; however, after loading with antibacterial/Mino, they exhibited strong antibacterial activity.

5. Conclusion

The present study has some limitations. Firstly, we have not fully explored the underlying therapeutic mechanism by which the drug-loaded nanoparticles regulate inflammation metabolism and oxidative stress. In addition, we did not consider the general condition of the whole body in DM. In the future, we will find solutions to the above problems and further focus on making the most of the diabetic microenvironment (e.g., high glucose and high level of ROS) to develop redox-responsive or glucose-responsive nanomaterials for the controlled release of drugs at the indicated points.

In conclusion, we constructed a novel drug delivery system based on DSPE-PEG-PAMAM, which was able to effectively co-deliver the antimicrobial/Mino and the antioxidant/ALA, disrupt dental-plaque biofilms, and suppress periodontal bone loss. This dual-drug delivery system has several advantages: (1) The ability to penetrate and be retained in local infected tissue, which is strongly dependent on their small size and surface charge. (2) High biocompatibility because DSPE-PEG has a similar structure to the cytomembrane. (3) High loading efficiency resulting from the unique core-shell and radiate dendritic structure harboring a large void space for the drug. (4) Multiple functions, mainly via loading with two kinds of specific and efficient drugs simultaneously. (5) pH and lipase-responsive abilities obtained by exploiting the specificity of the microenvironment. Considering these advantages, this drug delivery system implements precise measures and offers a promising strategy to treat periodontitis under DM conditions.

Data availability

The authors declare that all data supporting the findings of this study

are available within the paper and Supplementary Information.

CRediT authorship contribution statement

Lu Wang: Methodology, Formal analysis, Software, Analysis using software, Investigation, Writing – original draft. **Yuzhou Li:** Writing – review & editing, Resources. **Mingxing Ren:** Formal analysis, Visualization. **Xu Wang:** Formal analysis, Visualization. **Linjie Li:** Resources, Data curation. **Fengyi Liu:** Validation, Data curation. **Yiqing Lan:** Validation, Data curation. **Sheng Yang:** Supervision, Project administration, Conceptualization, Funding acquisition. **Jinlin Song:** Supervision, Project administration, Conceptualization, Funding acquisition.

Declaration of competing interest

The authors have no conflicts of interest to declare.

Acknowledgements

Appendix A. Supplementary data

Supplementary data to this article can be found online at https://doi.org/10.1016/j.bioactmat.2022.02.008.

References

[1] X. Sun, Z.J. Ma, X. Zhao, W.J. Jin, C.Y. Zhang, J. Ma, L. Qiang, W.H. Wang, Q. Deng, H. Yang, J.Z. Zhao, Q.Q. Liang, X.J. Zhou, L. Li, J. Wang, Three-dimensional bioprinting of multicell-laden scaffolds containing bone morphogenic protein-4 for promoting M2 macrophage polarization and accelerating bone defect repair in diabetes mellitus, Bioact Mater (3) (2020 Sep 25 6) 757–769.

[2] Y. Zheng, S.H. Ley, F.B. Hu, Global aetiology and epidemiology of type 2 diabetes mellitus and its complications, Nat. Rev. Endocrinol. 14 (2) (2018) 88–98.

[3] T. Kocher, J. Konig, W.S. Borgnakke, C. Pink, P. Meisel, Periodontal complications of hyperglycemia/diabetes mellitus: epidemiologic complexity and clinical challenge, Periodontol 78 (1) (2000) 59–97, 2018.

[4] M. Zheng, C. Wang, A. Ali, Y.A. Shih, Q. Xie, C. Guo, Prevalence of periodontitis in people clinically diagnosed with diabetes mellitus: a meta-analysis of epidemiologic studies, Acta Diabetol. (2021).

[5] D.T. Graves, Z. Ding, Y. Yang, The impact of diabetes on periodontal diseases, Periodontol 82 (1) (2000) 214–224, 2020.

[6] D. Polak, L. Shapira, An update on the evidence for pathogenic mechanisms that may link periodontitis and diabetes, J. Clin. Periodontol. 45 (2) (2018) 150–166.

[7] A.I. Khumaedi, D. Purnamasari, I.P. Wijaya, Y. Soeroso, The relationship of diabetes, periodontitis and cardiovascular disease, Diabetes Metab Syndr 13 (2) (2019) 1675–1678.

[8] M. Yamamoto, T. Sugimoto, Advanced glycation end products, diabetes, and bone strength, Curr. Osteoporos. Rep. 14 (6) (2016) 320–326.

[9] K. Asadipooya, E.M. Uy, Advanced glycation end products (AGEs), receptor for AGEs, diabetes, and bone: review of the literature, J Endocr Soc 3 (10) (2019) 1799–1818.

[10] T.C. Simpson, J.C. Weldon, H.V. Worthington, I. Needleman, S.H. Wild, D.R. Moles, B. Stevenson, S. Furness, Z. Iheozor-Ejiofor, Treatment of periodontal disease for glycaemic control in people with diabetes mellitus, Cochrane Database Syst. Rev. 11 (2015) CD004714.

[11] Y. Fan, M. Marioli, K. Zhang, Analytical characterization of liposomes and other lipid nanoparticles for drug delivery, J. Pharm. Biomed. Anal. 192 (2021) 113642.

[12] L.M. Ickenstein, P. Garidel, Lipid-based nanoparticle formulations for small molecules and RNA drugs, Expet Opin. Drug Deliv. 16 (11) (2019) 1205–1226.

[13] Y. Liu, K.M. Castro Bravo, J. Liu, Targeted liposomal drug delivery: a nanoscience and biophysical perspective, Nanoscale Horiz 6 (2) (2021) 78–94.

[14] Z. Wan, R. Zheng, P. Moharil, Y. Liu, J. Chen, R. Sun, X. Song, Q. Ao, Polymeric micelles in cancer immunotherapy, Molecules 26 (5) (2021).

[15] W. Zhang, A. Mehta, Z. Tong, L. Esser, N.H. Voelcker, Development of polymeric nanoparticles for blood-brain barrier transfer-strategies and challenges, Adv. Sci. 8 (10) (2021) 2003937.

[16] I. Aksoy, H. Kucukkececi, F. Sevgi, O. Metin, I. Hatay Patir, Photothermal antibacterial and antibiofilm activity of black phosphorus/gold nanocomposites against pathogenic bacteria, ACS Appl. Mater. Interfaces 12 (24) (2020) 26822–26831.

[17] Q. Zhao, J. Wang, C. Yin, P. Zhang, J. Zhang, M. Shi, K. Shen, Y. Xiao, Y. Zhao, X. Yang, Y. Zhang, Near-infrared light-sensitive nano neuro-immune blocker capsule relieves pain and enhances the innate immune response for necrotizing infection, Nano Lett. 19 (9) (2019) 5904–5914.

[18] S. Gomez-Grana, J. Perez-Juste, P. Herves, Cyclodextrins and inorganic nanoparticles: another tale of synergy, Adv. Colloid Interface Sci. 288 (2021) 102338.

[19] X. Li, X. Liu, X. Liu, Self-assembly of colloidal inorganic nanocrystals: nanoscale forces, emergent properties and applications, Chem. Soc. Rev. 50 (3) (2021) 2074–2101.

[20] S. Vieira, S. Vial, R.L. Reis, J.M. Oliveira, Nanoparticles for bone tissue engineering, Biotechnol. Prog. 33 (3) (2017) 590–611.

[21] A. Bozorgi, M. Khazaei, M. Soleimani, Z. Jamalpoor, Application of nanoparticles in bone tissue engineering; a review on the molecular mechanisms driving osteogenesis, Biomater Sci 9 (13) (2021) 4541–4567.

[22] Y. Wang, Q. Yuan, W. Feng, W. Pu, J. Ding, H. Zhang, X. Li, B. Yang, Q. Dai, L. Cheng, J. Wang, F. Sun, D. Zhang, Targeted delivery of antibiotics to the infected pulmonary tissues using ROS-responsive nanoparticles, J. Nanobiotechnol. 17 (1) (2019) 103.

[23] N. Jia, W. Li, D. Liu, S. Wu, B. Song, J. Ma, D. Chen, H. Hu, Tumor microenvironment stimuli-responsive nanoparticles for programmed anticancer drug delivery, Mol. Pharm. 17 (5) (2020) 1516–1526.

[24] U. Kauscher, M.N. Holme, M. Bjornmalm, M.M. Stevens, Physical stimuli-responsive vesicles in drug delivery: beyond liposomes and polymersomes, Adv. Drug Deliv. Rev. 138 (2019) 259–275.

[25] X. Mu, S. Gan, Y. Wang, H. Li, G. Zhou, Stimulus-responsive vesicular polymer nano-integrators for drug and gene delivery, Int. J. Nanomed. 14 (2019) 5415–5434.

[26] P.M. Preshaw, S.M. Bissett, Periodontitis and diabetes, Br. Dent. J. 227 (7) (2019) 577–584.

[27] A. Bascones-Martínez, M. Muñoz-Corcuera, J. Bascones-Ilundain, Diabetes and periodontitis: a bidirectional relationship, Med. Clínica 145 (1) (2015) 31–35.

[28] F. Hu, Z. Zhou, Q. Xu, C. Fan, L. Wang, H. Ren, S. Xu, Q. Ji, X. Chen, A novel pH-responsive quaternary ammonium chitosan-liposome nanoparticles for periodontal treatment, Int. J. Biol. Macromol. 129 (2019) 1113–1119.

[29] C.Y. Zhang, J. Gao, Z. Wang, Bioresponsive nanoparticles targeted to infectious microenvironments for sepsis management, Adv. Mater. 30 (43) (2018), e1803618.

[30] B. Horev, M.I. Klein, G. Hwang, Y. Li, D. Kim, H. Koo, D.S. Benoit, pH-activated nanoparticles for controlled topical delivery of farnesol to disrupt oral biofilm virulence, ACS Nano 9 (3) (2015) 2390–2404.

[31] Y. Gao, J. Wang, M. Chai, X. Li, Y. Deng, Q. Jin, J. Ji, Size and charge adaptive clustered nanoparticles targeting the biofilm microenvironment for chronic lung infection management, ACS Nano 14 (5) (2020) 5686–5699.

[32] Y. Liu, V.S. Bryantsev, M.S. Diallo, W.A. Goddard, PAMAM dendrimers undergo pH responsive conformational changes without swelling, J. Am. Chem. Soc. 131 (8) (2009) 2798–2799.

[33] L. Han, R.Q. Huang, S.H. Liu, S.X. Huang, C. Jiang, Peptide-conjugated PAMAM for targeted doxorubicin delivery to transferrin receptor overexpressed tumors, Mol. Pharm. 7 (2010) 2156–2165.

[34] G. Jiang, S. Liu, T. Yu, R. Wu, Y. Ren, H.C. van der Mei, J. Liu, H.J. Busscher, PAMAM dendrimers with dual-conjugated vancomycin and Ag-nanoparticles do not induce bacterial resistance and kill vancomycin-resistant Staphylococci, Acta Biomater. 123 (2021) 230–243.

[35] Y. Wang, Y. Luo, Q. Zhao, Z. Wang, Z. Xu, X. Jia, An enzyme-responsive nanogel carrier based on PAMAM dendrimers for drug delivery, ACS Appl. Mater. Interfaces 8 (31) (2016) 19899–19906.

[36] Y. Zhang, S. Ma, X. Liu, Y. Xu, J. Zhao, X. Si, H. Li, Z. Huang, Z. Wang, Z. Tang, W. Song, X. Chen, Supramolecular assembled programmable nanomedicine as in situ cancer vaccine for cancer immunotherapy, Adv. Mater. 33 (7) (2021), e2007293.

[37] A.S. Chauhan, Dendrimers for drug delivery, Molecules 23 (4) (2018).

[38] H. Kheraldine, O. Rachid, A.M. Habib, A.E. Al Moustafa, I.F. Benter, S. Akhtar, Emerging innate biological properties of nano-drug delivery systems: a focus on PAMAM dendrimers and their clinical potential, Adv. Drug Deliv. Rev. 178 (2021) 113908.

[39] L. Aranda-Lara, B.E.O. Garcia, K. Isaac-Olive, G. Ferro-Flores, L. Melendez-Alafort, E. Morales-Avila, Drug delivery systems-based dendrimers and polymer micelles for nuclear diagnosis and therapy, Macromol. Biosci. 21 (3) (2021), e2000362.

[40] Z. Zeng, D. Qi, L. Yang, J. Liu, Y. Tang, H. Chen, X. Feng, Stimuli-responsive self-assembled dendrimers for oral protein delivery, J. Contr. Release 315 (2019) 206–213.

[41] D. Huang, D. Wu, Biodegradable dendrimers for drug delivery, Mater Sci Eng C Mater Biol Appl 90 (2018) 713–727.

[42] M. Chen, S. Xie, J. Wei, X. Song, Z. Ding, X. Li, Antibacterial micelles with vancomycin-mediated targeting and pH/lipase-triggered release of antibiotics, ACS Appl. Mater. Interfaces 10 (43) (2018) 36814–36823.

[43] V.M. Barnes, S.G. Ciancio, O. Shibly, T. Xu, W. Devizio, H.M. Trivedi, L. Guo, T. J. Jonsson, Metabolomics reveals elevated macromolecular degradation in periodontal disease, J. Dent. Res. 90 (11) (2011) 1293–1297.

[44] J. Che, C.I. Okeke, Z.B. Hu, J. Xu, DSPE-PEG: a distinctive component in drug delivery system, Curr. Pharmaceut. Des. 21 (12) (2015) 1598–1605.

[45] A.T. Wang, D.S. Liang, Y.J. Liu, X.R. Qi, Roles of ligand and TPGS of micelles in regulating internalization, penetration and accumulation against sensitive or resistant tumor and therapy for multidrug resistant tumors, Biomaterials 53 (2015) 160–172.

[46] B. Salehi, Y. Berkay Yilmaz, G. Antika, T. Boyunegmez Tumer, M. Fawzi Mahomoodally, D. Lobine, M. Akram, M. Riaz, E. Capanoglu, F. Sharopov, N. Martins, W.C. Cho, J. Sharifi-Rad, Insights on the use of alpha-lipoic acid for therapeutic purposes, Biomolecules 9 (8) (2019).

[47] R. Jagannathan, J.S. Neves, B. Dorcely, S.T. Chung, K. Tamura, M. Rhee, M. Bergman, The oral glucose tolerance test: 100 Years later, Diabetes Metab Syndr Obes 13 (2020) 3787–3805.

[48] T. Wei, C. Chen, J. Liu, C. Liu, P. Posocco, X. Liu, Q. Cheng, S. Huo, Z. Liang, M. Fermeglia, S. Pricl, X.J. Liang, P. Rocchi, L. Peng, Anticancer drug nanomicelles formed by self-assembling amphiphilic dendrimer to combat cancer drug resistance, Proc. Natl. Acad. Sci. U. S. A. 112 (10) (2015) 2978–2983.

[49] H. Van Acker, T. Coenye, The role of reactive oxygen species in antibiotic-mediated killing of bacteria, Trends Microbiol. 25 (6) (2017) 456–466.

[50] F. Vatansever, W.C. de Melo, P. Avci, D. Vecchio, M. Sadasivam, A. Gupta, R. Chandran, M. Karimi, N.A. Parizotto, R. Yin, G.P. Tegos, M.R. Hamblin, Antimicrobial strategies centered around reactive oxygen species–bactericidal antibiotics, photodynamic therapy, and beyond, FEMS Microbiol. Rev. 37 (6) (2013) 955–989.

[51] P. Ma, H. Xiao, C. Yu, J. Liu, Z. Cheng, H. Song, X. Zhang, C. Li, J. Wang, Z. Gu, J. Lin, Enhanced cisplatin chemotherapy by iron oxide nanocarrier-mediated generation of highly toxic reactive oxygen species, Nano Lett. 17 (2) (2017) 928–937.

[52] M. Freitas, J.L. Lima, E. Fernandes, Optical probes for detection and quantification of neutrophils' oxidative burst, A review, Anal Chim Acta 649 (1) (2009) 8–23.

[53] Y. Chen, W.G. Junger, Measurement of oxidative burst in neutrophils, Methods Mol. Biol. 844 (2012) 115–124.

[54] D.C. Thomas, The phagocyte respiratory burst: historical perspectives and recent advances, Immunol. Lett. 192 (2017) 88–96.

[55] L. Sui, J. Wang, Z. Xiao, Y. Yang, Z. Yang, K. Ai, ROS-scavenging nanomaterials to treat periodontitis, Front. Chem. 8 (2020) 595530.

[56] W. Liu, L.J. Shi, S.G. Li, The immunomodulatory effect of alpha-lipoic acid in autoimmune diseases, BioMed Res. Int. 2019 (2019) 8086257.

[57] V.M. Mendoza-Nunez, B.I. Garcia-Martinez, J. Rosado-Perez, E. Santiago-Osorio, J. Pedraza-Chaverri, V.J. Hernandez-Abad, The effect of 600 mg alpha-lipoic acid supplementation on oxidative stress, inflammation, and RAGE in older adults with type 2 diabetes mellitus, Oxid. Med. Cell. Longev. (2019) 3276958, 2019.

[58] U. Aksoy, G. Savtekin, A.O. Sehirli, F. Kermeoglu, A. Kalender, H. Ozkayalar, S. Sayiner, K. Orhan, Effects of alpha-lipoic acid therapy on experimentally induced apical periodontitis: a biochemical, histopathological and micro-CT analysis, Int. Endod. J. 52 (9) (2019) 1317–1326.